RESEARCH ARTICLE

National Science Review
5: 507–515, 2018
doi: 10.1093/nsr/nwy033
Advance access publication 12 March 2018

CHEMISTRY

Manipulation of successive crystalline transformations to control electron transfer and switchable functions

Cheng-Qi Jiao[1], Wen-Jing Jiang[1], Yin-Shan Meng[1], Wen Wen[1], Liang Zhao[1], Jun-Li Wang[1], Ji-Xiang Hu[1], Gagik G. Gurzadyan[2], Chun-Ying Duan[1] and Tao Liu[1,*]

ABSTRACT

Electron transfer in solid is crucial to switchable magnetic, electrical, optical and mechanical properties. However, it is a formidable challenge to control electron-transfer behaviors via manipulation of crystalline phases, especially through dynamic crystalline transformation. Herein, three crystalline phases of an $\{Fe_2Co_2\}$ compound were obtained via enhancement of intermolecular $\pi\cdots\pi$ interactions inducing successive single-crystal-to-single-crystal transformations, from solvated **1·2CH$_3$OH·4H$_2$O**, to desolvated **1** and its polymorph **1a** accompanying electron transfer. **1·2CH$_3$OH·4H$_2$O** showed thermally induced reversible intermetallic electron transfer in mother liquor. No electron-transfer behavior was observed in **1**. **1a** showed reversible intermetallic electron transfer upon thermal treatment or alternative irradiation with 808- and 532-nm lasers at cryogenic temperatures. The electron-transfer behaviors significantly change the magnetic and optical properties, providing a strategy to realize different electron-transfer behaviors and switchable functions via $\pi\cdots\pi$ interactions manipulated dynamic crystalline transformation.

Keywords: electron-transfer, dynamic structural transformation, successive crystalline transformations, reversible, polymorphs

INTRODUCTION

Electron transfer is a common phenomenon in nature and plays important roles in biology, energy, materials, catalysis and other fields [1–4]. Intermetallic electron transfer not only changes the valence states and electron configurations of the participant metal ions, but also switches the coupling interactions between them [2,5–7]. Therefore, the control of electron transfer is an efficient way to tune the magnetic, electric and optical properties of materials [8–22]. Thermally and/or photo-induced electron transfers have been utilized to induce paramagnetic and diamagnetic transformations, presenting photo-switchable magnet behavior [11–13]. Moreover, the polarity and dielectric properties can be switched by utilizing electron-transfer-induced changes in charge distribution [23,24].

Typical examples showing external stimuli-tuned intermetallic electron-transfer behaviors are cyanide-bridged complexes, wherein the electron-transfer behaviors depend on the metallocyanate building blocks and ancillary ligands [11]. The modulation of electron-transfer behavior requires chemical modification, such as ligand substitution, anion and solvent exchange in solution reaction [11,17,20]. It is a formidable challenge to realize different electron-transfer behaviors by manipulating dynamic structural transformations in the solid state, especially through physical stimuli-induced single-crystal-to-single-crystal (SCSC) transformations. Such transformation processes usually involve the movement of atoms in the crystal and rearrangement of chemical bonds, which result in drastic changes in not only the molecular structure, but also the physical/chemical properties [25–28]. On the other hand, SCSC transformations can provide access to compounds that are difficult or impossible to be directly obtained by solution reactions [28]. More importantly, the procedure of SCSC transformations can directly and accurately provide a molecular-level understanding of the mechanism of the transformation, and help to gain more insights into the correlation between the structures and properties [29,30].

[1]State Key Laboratory of Fine Chemicals, Dalian University of Technology, Dalian 116024, China and [2]Institute of Artificial Photosynthesis, State Key Laboratory of Fine Chemicals, Dalian University of Technology, Dalian 116024, China

*Corresponding author. E-mail: liutao@dlut.edu.cn

Received 5 December 2017; **Revised** 1 February 2018; **Accepted** 8 March 2018

It has been reported that two crystalline phases with different electron-transfer behaviors could be obtained upon solvation and desolvation, because hydrogen-bonding interactions between coordinated solvents and the framework can tune the redox potentials of metal ions [31–36]. However, the formation and breakage of hydrogen bonds could only induce one-step SCSC transformation and generate two crystalline phases with different electron-transfer behaviors [32–36]. Moreover, the crystallinity is often disrupted owing to breakage of the hydrogen-bonding interactions that are important to maintain the integrity of the crystalline framework [25,31], restricting further investigation of the electron-transfer mechanism. How to induce successive crystalline transformation to obtain more than two crystalline phases with different electron-transfer behaviors is interesting but still remains a challenge, especially for polymorphs with different electron-transfer behaviors. To induce successive SCSC transformations, introducing flexible $\pi\cdots\pi$ interactions may provide a rational strategy [9,37], as the distances of $\pi\cdots\pi$ interactions can be modulated in a continuous range (3.3–3.8 Å) [38]. Moreover, the variations in $\pi\cdots\pi$ interactions between ligands around the metal ions can induce different distortions of coordination spheres and the strength of the ligand field, which can tune the redox potential of metal centers and result in different electron-transfer behaviors.

Herein, we were intrigued by the possibility of introducing intermolecular cooperative $\pi\cdots\pi$ interactions to manipulate successive crystalline transformations to obtain different crystalline phases featuring different electron-transfer behaviors. Inspired by this, we adopt an ancillary ligand prazino[2, 3-f][1, 10]phenanthroline (dpq), with an extended π-conjugation system, to prepare a tetranuclear $\{Fe_2Co_2\}$ compound $[Fe^{II}(^{Pz}Tp)(CN)_3]_2Co^{III}{}_2(dpq)_4\cdot 2ClO_4\cdot 2CH_3OH\cdot 4H_2O$ (**1·2CH$_3$OH·4H$_2$O**, ^{Pz}Tp = tetrakis (pyrazolyl)borate). **1·2CH$_3$OH·4H$_2$O** undergoes successive SCSC transformations as a result of enhancement of intermolecular $\pi\cdots\pi$ interactions in the process of desolvation and structural rearrangement, forming a pair of polymorphs $[Fe^{III}(^{Pz}Tp)(CN)_3]_2Co^{II}{}_2(dpq)_4\cdot 2ClO_4$ (**1**) and $[Fe^{II}(^{Pz}Tp)(CN)_3]_2Co^{III}{}_2(dpq)_4\cdot 2ClO_4$ (**1a**). The three crystalline phases present different electron-transfer behaviors upon thermal treatment and light irradiation. Especially, it is the first time that crystalline transformation between a pair of polymorphs in intermetallic electron-transfer-related compounds has been observed.

RESULTS

Crystal structure of 1·2CH$_3$OH·4H$_2$O and its successive crystalline transformations

Single-crystal X-ray diffraction analysis revealed that **1·2CH$_3$OH·4H$_2$O** crystallizes in the triclinic space group $P\bar{1}$ (see Supplementary Table 1). The crystal structure consists of cationic tetranuclear $\{Fe_2Co_2\}^{2+}$ square units, ClO_4^- anions, uncoordinated methanol and water molecules (Fig. 1). At 298 K, the Fe–C and Co–N bond lengths are 1.877(7)–1.889(7) and 1.879(5)–1.946(5) Å, respectively (see Supplementary Table 2), which are consistent with those observed for $\{Fe^{II}{}_{LS}(\mu\text{-}CN)Co^{III}{}_{LS}\}$ (LS = low spin) linkages [17,33]. When the green crystals are slowly heated to 360 K in the mother liquor, a dramatic color change from green to red is observed, indicating a possible transformation to $\{Fe^{III}{}_{LS}(\mu\text{-}CN)Co^{II}{}_{HS}\}$ (HS = high spin) linkages. On cooling to 298 K, the crystals return to the initial green color. This phenomenon indicates that **1·2CH$_3$OH·4H$_2$O** undergoes a thermally induced reversible electron transfer in the mother liquor (see Supplementary Movie 1).

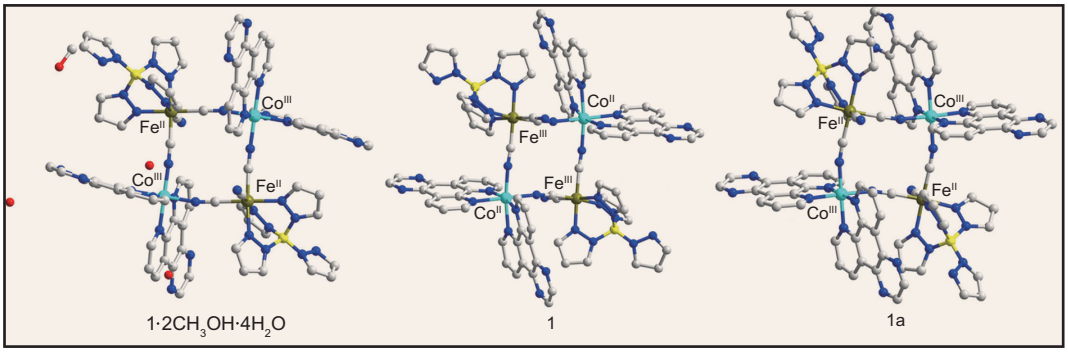

Figure 1. Crystal structures of **1·2CH$_3$OH·4H$_2$O**, **1** and **1a**. The hydrogen atoms and ClO_4^- anions are omitted for clarity. Fe, dark yellow; Co, turquoise; C, gray; N, blue; B, orange; O, red.

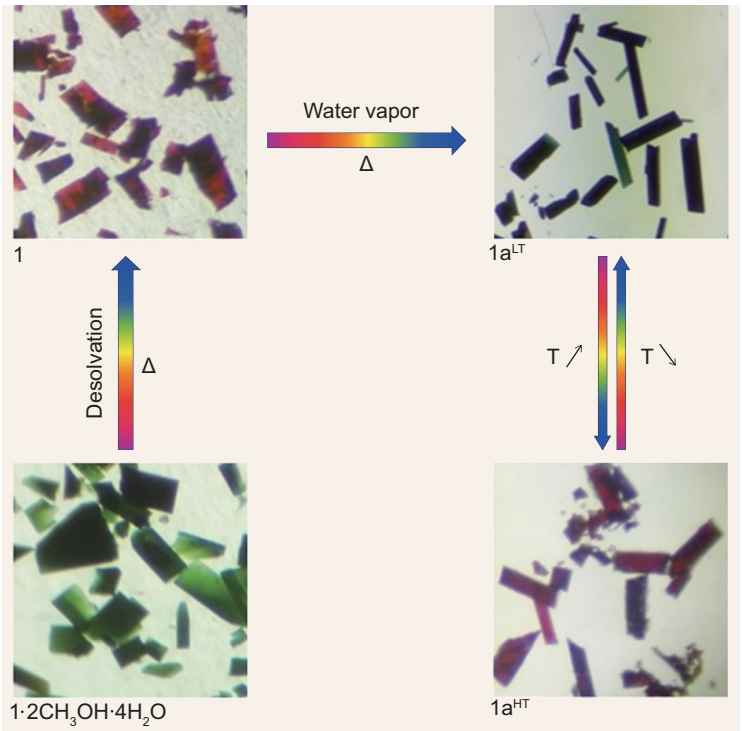

Figure 2. Photographic images showing the SCSC transformation. Images show the conversions among these three species through subsequent desolvation and vapor induction.

There are two important structural characteristics in **1·2CH$_3$OH·4H$_2$O**. The first is that uncoordinated water and methanol molecules are located between the $\{Fe_2Co_2\}^{2+}$ square units, with hydrogen-bonding interactions between uncoordinated water molecules and terminal cyanide nitrogen atoms (see Supplementary Fig. 1 and Table 4). The second is that the $\{Fe_2Co_2\}^{2+}$ square units are linked via $\pi\cdots\pi$ interactions (average distance = 3.753(2) Å) between the dpq ligands and C–H$\cdots\pi$ interactions (average distance = 3.148(1) Å) between the C–H moieties of the dpq/^{Pz}Tp ligands and the pyrazol/pyrazine rings of the ^{Pz}Tp/dpq ligands (see Supplementary Fig. 2 and Table 5). These intermolecular interactions are very important to stabilize the crystalline framework and make it possible to undergo SCSC transformations upon desolvation. Furthermore, the formation and destruction of hydrogen bonding can significantly affect the redox potential of the iron centers [31,33], providing the possibility of desolvation-induced electron transfer. Thus, two crystalline phases with different electron-transfer behaviors are reasonably expected.

The TGA (see Supplementary Fig. 3) of **1·2CH$_3$OH·4H$_2$O** was measured to explore the possibility of desolvation-induced SCSC transformation. The plot shows a weight loss of 6.0% from 300 to 360 K, corresponding well to the loss of two methanol and four water molecules (calcd: 6.2%). After this weight loss, a long plateau is observed until 540 K, suggesting the formation of a new stable phase. When the green crystals are slowly heated to ∼350 K in air, the color of the crystals changes from green to red, indicating the formation of a new redox state. Moreover, the crystallinity is well retained (Fig. 2 and see Supplementary Movie 2). The crystallographic data demonstrate that the red crystals retain the $\{Fe_2Co_2\}$ tetranuclear structure and have the formula of $[Fe(^{Pz}Tp)(CN)_3]_2Co_2(dpq)_4\cdot 2ClO_4$ (**1**, Fig. 1). At 298 K, the Fe–C and Co–N bond lengths are 1.925(8)–1.944(9) and 2.097(7)–2.169(7) Å, respectively (see Supplementary Table 2), corresponding with those observed for $\{Fe^{III}_{LS}(\mu\text{-CN})Co^{II}_{HS}\}$ linkages [17,39]. These results indicate that electron transfer occurs in the desolvation process with a transformation from $\{Fe^{II}_{LS}(\mu\text{-CN})Co^{III}_{LS}\}$ linkages in **1·2CH$_3$OH·4H$_2$O** to $\{Fe^{III}_{LS}(\mu\text{-CN})Co^{II}_{HS}\}$ linkages in **1**. Furthermore, an endothermic peak is seen in the DSC curve of **1·2CH$_3$OH·4H$_2$O**, further confirming the first-order phase transition from **1·2CH$_3$OH·4H$_2$O** to **1** (see Supplementary Fig. 4). With the transformation from **1·2CH$_3$OH·4H$_2$O** to **1**, the average $\pi\cdots\pi$ interaction distance between the dpq ligands decreases from 3.753(2) to 3.664(1) Å, and the average C–H$\cdots\pi$ interaction distance between the C–H moieties of the dpq/^{Pz}Tp ligands and the pyrazol rings of the ^{Pz}Tp ligands decreases from 3.148(1) to 3.102(1) Å. Such results suggest that the intermolecular interactions are enhanced in the process of crystalline transformation (see Supplementary Fig. 5 and Table 6).

Interestingly, when the red crystals of **1** were placed in water vapor and heated at 100°C for 24 h, the color of the crystals changed from red to green (Fig. 2, see Supplementary Fig. 6), suggesting the formation of a new phase, as confirmed by single-crystal X-ray diffraction (Fig. 1) and powder XRD analyses (see Supplementary Fig. 7). The new phase exhibits a composition consistent with the formula $[Fe(^{Pz}Tp)(CN)_3]_2Co_2(dpq)_4\cdot 2ClO_4$ (**1a**). Although **1** and **1a** are a pair of polymorphs, they exhibit different electron-transfer behaviors. For **1a** at 298 K, the Fe–C and Co–N bond lengths are 1.852(4)–1.914(4) and 1.877(3)–1.949(3) Å, respectively (see Supplementary Table 2), indicating the existence of $\{Fe^{II}_{LS}(\mu\text{-CN})Co^{III}_{LS}\}$ linkages. When the crystals of **1a** are slowly heated to 350 K, a dramatic color change from green to red is observed. The corresponding Co–N bond lengths are 2.077(4)–2.145(3) Å (see Supplementary Table 2), indicating the formation of $\{Fe^{III}_{LS}(\mu\text{-CN})Co^{II}_{HS}\}$ linkages [17,39]. Moreover, the crystals return to the initial green color on cooling to

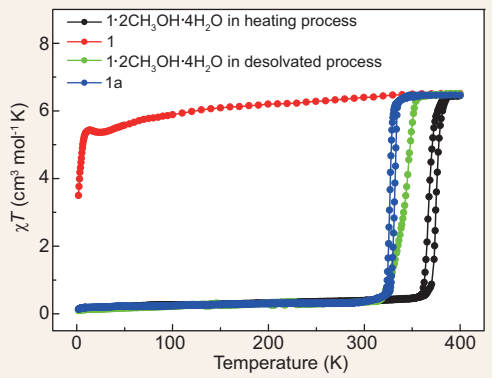

Figure 3. Magnetic characteristics for **1·2CH$_3$OH·4H$_2$O**, **1** and **1a**. Plots of χT vs temperature for **1·2CH$_3$OH·4H$_2$O**, **1** and **1a**. **1·2CH$_3$OH·4H$_2$O** was soaked in the mother liquor upon cooling, and cycling the temperature back to 400 K; **1** upon cooling; **1·2CH$_3$OH·4H$_2$O** upon heating and concomitant desorption of methanol and water; **1a** upon cooling and reheating to 400 K (temperature sweeping rate: 1 K/min for 10–400 K and 0.5 K/min for 2–10 K).

298 K, indicating the thermally induced reversible intermetallic electron transfer. With the transformation from **1** to **1a**, the average $\pi\cdots\pi$ interaction distance between the dpq ligands decreases from 3.664(1) to 3.457(1) Å at room temperature, and the average C–H$\cdots\pi$ interaction distance between the C–H moieties of the dpq/^{Pz}Tp ligands and the pyrazol/pyridine rings of the ^{Pz}Tp/dpq ligands decreases from 3.102(1) to 3.002(1) Å, leading to the enhanced intermolecular interactions (see Supplementary Fig. 8 and Table 7). When heated to 350 K, both the average $\pi\cdots\pi$ interaction and C–H$\cdots\pi$ interaction distances of **1a** increase slightly (see Supplementary Fig. 9 and Table 8).

Magnetic characterization

The magnetic properties of the three crystalline phases were subsequently investigated (Fig. 3). The χT versus T curve for **1·2CH$_3$OH·4H$_2$O** in mother liquor shows that χT values remain essentially constant at 0.46 cm^3 mol^{-1} K below 355 K, confirming the existence of $\{Fe^{II}_{LS}(\mu\text{-CN})Co^{III}_{LS}\}$ linkages. Upon heating, χT values abruptly increase to 6.44 cm^3 mol^{-1} K at 390 K, which are in agreement with the theoretical value of 6.67 cm^3 mol^{-1} K expected for two LS Fe^{III} and two HS Co^{II} ions [16]. When the temperature is lowered from 400 K, χT values decrease rapidly to its initial value at 355 K with a small thermal hysteresis loop of ~8 K, indicating that the system regains the $\{Fe^{II}_{LS}(\mu\text{-CN})Co^{III}_{LS}\}$ linkages. Thus, **1·2CH$_3$OH·4H$_2$O** shows thermally induced reversible intermetallic electron transfer upon thermal treatment in the mother liquor.

However, **1** exhibits a different electron-transfer behavior. Its χT value is 6.51 cm^3 mol^{-1} K at 400 K (Fig. 3), corresponding to paramagnetic $\{Fe^{III}_{LS}(\mu\text{-CN})Co^{II}_{HS}\}$ linkages. As the temperature is lowered, χT values gradually decrease, reaching a minimum value of 5.36 cm^3 mol^{-1} K at 24 K. Below this temperature, the χT value increases up to 5.44 cm^3 mol^{-1} K at 14 K and then decreases rapidly to 3.50 cm^3 mol^{-1} K at 2 K. This represents a typical paramagnetic behavior without electron-transfer-induced spin transition. The transformation of the magnetic behavior in the desolvation process was monitored for as-synthesized crystals of **1·2CH$_3$OH·4H$_2$O**. χT values remain essentially constant at 0.36 cm^3 mol^{-1} K below 310 K and reach a maximum value of 6.43 cm^3 mol^{-1} K at 360 K, which is in agreement with paramagnetic $\{Fe^{III}_{LS}(\mu\text{-CN})Co^{II}_{HS}\}$ linkages as observed for **1**. Such magnetic behavior confirms that the electron transfer occurs in the desolvation process from **1·2CH$_3$OH·4H$_2$O** to **1**. This electron-transfer process seems analogous to that observed during the heating of **1·2CH$_3$OH·4H$_2$O** in mother liquor, but with a lower transition temperature. This is due to the difference in the intermetallic electron-transfer mechanism, as the former stems from the loss of solvent molecules, while the latter arises from thermal stimuli.

For **1a**, χT values remain nearly constant between 2 and 315 K at 0.43 cm^3 mol^{-1} K (Fig. 3). Heating from 315 to 360 K causes an increase in the χT value to 6.47 cm^3 mol^{-1} K. The χT value returns to its initial value with a small thermal hysteresis ~5 K wide, showing reversible electron-transfer behavior that involves transformation between the diamagnetic $\{Fe^{II}_{LS}(\mu\text{-CN})Co^{III}_{LS}\}$ (LT phase = low temperature phase) linkages and the paramagnetic $\{Fe^{III}_{LS}(\mu\text{-CN})Co^{II}_{HS}\}$ (HT phase = high temperature phase) linkages. Consistently with magnetic data, endothermic/exothermic peaks for **1a** are observed with T_{max} = 331.2 and 325.3 K, indicating the occurrence of the first-order phase transition (see Supplementary Fig. 10).

Optical studies

The solid-state UV–vis–NIR absorption spectra of **1·2CH$_3$OH·4H$_2$O**, **1** and **1a** were measured at room temperature to study their color changes and to further support the electronic state assignments deduced from the structural and magnetic analyses (Fig. 4a). The absorption spectra of **1·2CH$_3$OH·4H$_2$O** and **1a** are similar, presenting bands at 427 and 763 nm, respectively. The absorption band at 427 nm may be assigned to ligand-to-metal charge transfer (LMCT) of the Fe^{II} chromophore [17]. The broad band at 763 nm can be

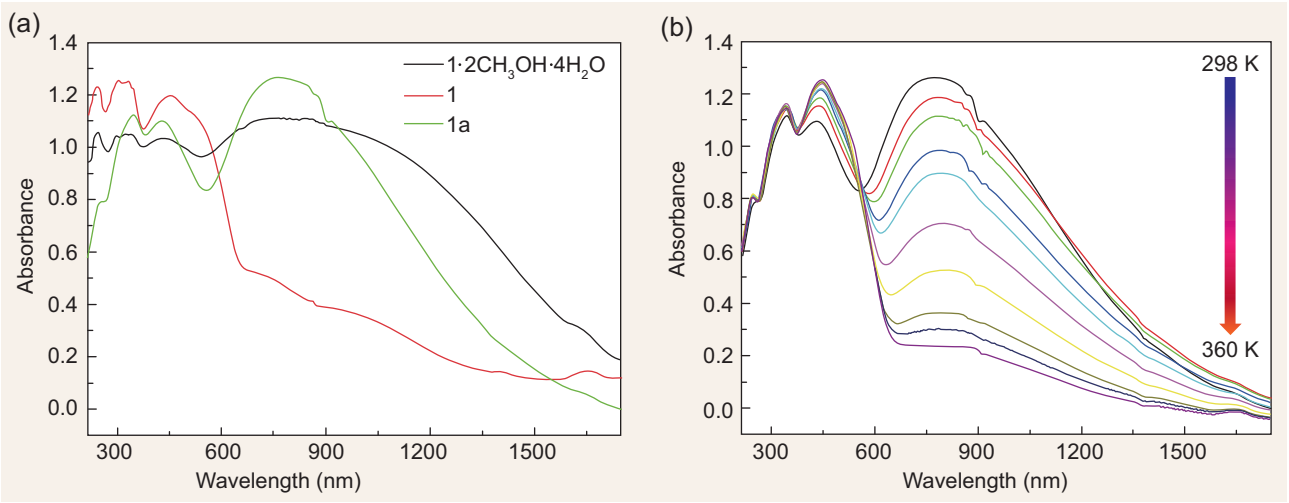

Figure 4. Optical spectra for **1·2CH$_3$OH·4H$_2$O**, **1** and **1a**. (a) Solid-state UV–vis spectra for **1·2CH$_3$OH·4H$_2$O**, **1** and **1a** at room temperature. (b) Variable-temperature solid-state UV–vis spectra for **1a** in heating (298→360 K) mode.

assigned as the $Fe^{II} \rightarrow Co^{III}$ intervalence charge-transfer (IVCT) band [17,35]. In contrast, a broad absorption band at 459 nm with a small shoulder band at 534 nm is observed for **1**. The higher-energy band at 459 nm is assigned to a spin- and Laporte-allowed LMCT transition, and the small shoulder band at 534 nm can be assigned to the $Co^{II} \rightarrow Fe^{III}$ IVCT band [39]. These results confirm that **1·2CH$_3$OH·4H$_2$O** and **1a** possess the diamagnetic $\{Fe^{II}_{LS}(\mu\text{-CN})Co^{III}_{LS}\}$ linkages, whereas **1** possesses the paramagnetic $\{Fe^{III}_{LS}(\mu\text{-CN})Co^{II}_{HS}\}$ linkages at room temperature.

Variable-temperature solid-state UV–vis–NIR absorption spectra of **1a** were measured in the temperature range of 298–360 K (Fig. 4b). As the temperature increases, there is a gradual decrease in the broad absorption centered at 763 nm for the characteristic band of the $Fe^{II} \rightarrow Co^{III}$ IVCT, and the LMCT/MLCT band at 427 nm is shifted to the lower-energy region associated with the appearance of the $Co^{II} \rightarrow Fe^{III}$ IVCT band at 527 nm. The observed spectral change confirms the occurrence of thermally induced electron transfer with the transformation from the $\{Fe^{II}_{LS}(\mu\text{-CN})Co^{III}_{LS}\}$ to $\{Fe^{III}_{LS}(\mu\text{-CN})Co^{II}_{HS}\}$ linkages.

Photomagnetic characterization

The photomagnetic effects of **1a** were examined to determine the possibility of photo-induced electron transfer. Because an $Fe^{II} \rightarrow Co^{III}$ IVCT band was observed at 763 nm for the LT phase of **1a**, an 808 nm laser was selected to stimulate the $Fe^{II} \rightarrow Co^{III}$ IVCT band and used for photomagnetic experiments. When the sample is irradiated at 20 K for 120 min, χT values rapidly increase and reach a maximum value of 5.61 cm^3 mol^{-1} K (Fig. 5a). When the sample is heated from 2 K after irradiation, χT values first increase steeply to a sharp maximum of 6.38 cm^3 mol^{-1} K at 8.2 K, indicating an almost complete conversion from diamagnetic $\{Fe^{II}_{LS}(\mu\text{-CN})Co^{III}_{LS}\}$ to paramagnetic $\{Fe^{III}_{LS}(\mu\text{-CN})Co^{II}_{HS}\}$ linkages (Fig. 5b). The increase in χT values from 2 to 8.2 K is attributed to the presence of intermolecular antiferromagnetic interactions and/or zero field splitting [16]. Upon further heating to 73 K, the photo-induced metastable paramagnetic $\{Fe^{III}_{LS}(\mu\text{-CN})Co^{II}_{HS}\}$ linkages relax to the initial diamagnetic $\{Fe^{II}_{LS}(\mu\text{-CN})Co^{III}_{LS}\}$ linkages, indicating that magnetization can be increased by light irradiation and recovered with thermal treatment.

On the basis of the optical studies, **1a** in HT phase displays a $Co^{II} \rightarrow Fe^{III}$ IVCT band at 527 nm. The photo-induced metastable phase after irradiation with an 808 nm laser was further irradiated with a 532 nm laser in order to investigate the photo-induced reversibility. As a result, χT values decrease from 5.61 to 2.27 cm^3 mol^{-1} K after 120 min irradiation at 20 K (Fig. 5b), indicating 59.5% recovery of the diamagnetic state. This successive photoreversibility of the magnetization can be well repeated (Fig. 5a and see Supplementary Fig. 11). This magnetic change verifies the occurrence of photo-induced reversible electron transfer in **1a**. The relaxation of the photo-induced metastable state was monitored at different temperatures in order to probe the stability of the photo-induced phases (see Supplementary Fig. 12). In the low-temperature (10–40 K) region, relaxation time τ was less dependent on temperature. This result additionally

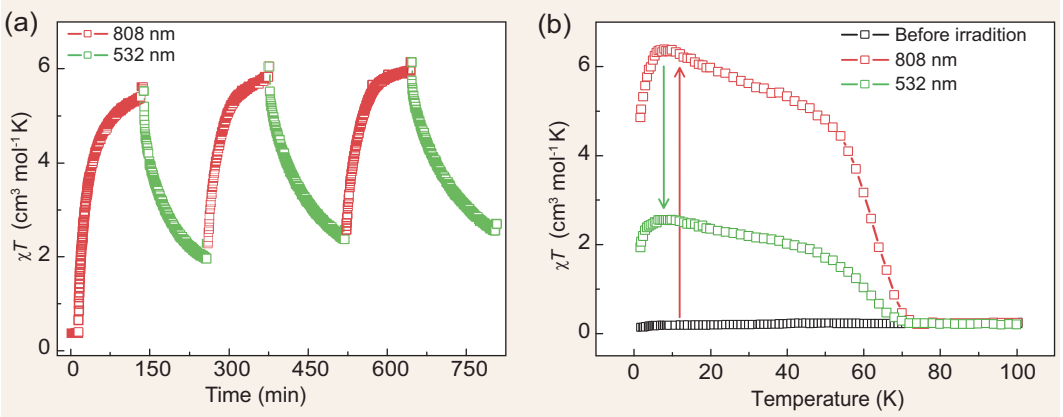

Figure 5. Photoreversibility of the magnetization for **1a**. (a) Plots of χT vs time under cycles of successive irradiation at 808 and 532 nm at 20 K for **1a**. (b) Plots of χT vs temperature for **1a** before irradiation, after irradiation at 808 nm, the metastable-induced state irradiated at 532 nm, and after thermal annealing treatment at 100 K.

confirms that the photoreversibility changes were induced by light rather than the thermal relaxation effect.

IR spectra

The IR spectra analysis of **1·2CH$_3$OH·4H$_2$O**, **1** and **1a** also supports the redox state assignments deduced from the structural and magnetic analyses. For **1·2CH$_3$OH·4H$_2$O**, the typical absorption bands of cyanide groups (2107, 2089 and 2071 cm^{-1}, see Supplementary Fig. 13) indicate that the compound possesses the diamagnetic $\{Fe^{II}_{LS}(\mu\text{-CN})Co^{III}_{LS}\}$ linkages [17,33]. Three absorption bands for cyanide groups are observed in the IR spectrum of **1** (see Supplementary Fig. 13), corresponding to the stretching vibrations for the bridging cyanide ions in the $\{Fe^{III}_{LS}(\mu\text{-CN})Co^{II}_{HS}\}$ linkages (2148 and 2143 cm^{-1}) and the terminal cyanide ions in the $[^{Pz}TpFe^{III}(CN)_3]^-$ anions (2122 cm^{-1}) [20]. At 300 K, **1a** shows absorption bands at 2069, 2085 and 2106 cm^{-1}, confirming that **1a** possesses the $\{Fe^{II}_{LS}(\mu\text{-CN})Co^{III}_{LS}\}$ linkages in the LT phase (see Supplementary Fig. 14). When the temperature increases to 360 K, the intensity of the cyanide stretching bands for the $\{Fe^{II}_{LS}(\mu\text{-CN})Co^{III}_{LS}\}$ linkages decreases, and new bands for the $\{Fe^{III}_{LS}(\mu\text{-CN})Co^{II}_{HS}\}$ linkages appear at 2150 and 2159 cm^{-1} as seen in **1**. Furthermore, upon cooling to room temperature, the IR spectra of **1a** return to their initial state, suggesting that the thermally induced intermetallic electron transfer is reversible.

The irradiation-time dependence of the IR spectra was measured to further verify the occurrence of photo-induced reversible electron transfer in **1a** upon successive and alternative irradiation with 808 and 532 nm lasers at 20 K (Fig. 6). Upon irradiation at 808 nm, the intensity of the cyanide stretching bands attributed to the $\{Fe^{II}_{LS}(\mu\text{-CN})Co^{III}_{LS}\}$ linkages decreases and a new peak appears at 2162 cm^{-1}, which is attributed to the $\{Fe^{III}_{LS}(\mu\text{-CN})Co^{II}_{HS}\}$ linkages. The intensity of the new peak gradually increases with irradiation time. Conversely, the photo-induced metastable phase was irradiated at 532 nm, inducing a decrease in the intensity of the cyanide stretching band attributed to the $\{Fe^{III}_{LS}(\mu\text{-CN})Co^{II}_{HS}\}$ linkages, and the intensity of the peaks attributed to the $\{Fe^{II}_{LS}(\mu\text{-CN})Co^{III}_{LS}\}$ linkages increases. By normalization of the peak intensities for the $\{Fe^{III}_{LS}(\mu\text{-CN})Co^{II}_{HS}\}$ linkages vs irradiation time upon irradiation at 808 and 532 nm, the recovery of the $\{Fe^{II}_{LS}(\mu\text{-CN})Co^{III}_{LS}\}$ linkages is estimated to be 60.0%, which is comparable to the value obtained from photomagnetic measurements (see Supplementary Fig. 15). Therefore, the observed spectral changes further confirm the occurrence of photo-induced reversible electron transfer with interconversion between $\{Fe^{III}_{LS}(\mu\text{-CN})Co^{II}_{HS}\}$ and $\{Fe^{II}_{LS}(\mu\text{-CN})Co^{III}_{LS}\}$ linkages through successive and alternative irradiation at 808 and 532 nm.

Structure and property discussion

Air-stable **1a** can be obtained by two-step-wise SCSC transformations from the air-unstable **1·2CH$_3$OH·4H$_2$O**. This unprecedented successive single-crystalline transformations-induced electron transfer inspired us to investigate their structural correlations. First, the structure of **1·2CH$_3$OH·4H$_2$O** indicates that hydrogen-bonding interactions are formed between the nitrogen atom of the terminal cyanide and an uncoordinated water molecule with the N···O distance of 2.713(12) Å (see Supplementary Fig. 1 and Table 4). Hydrogen-bonding strength can

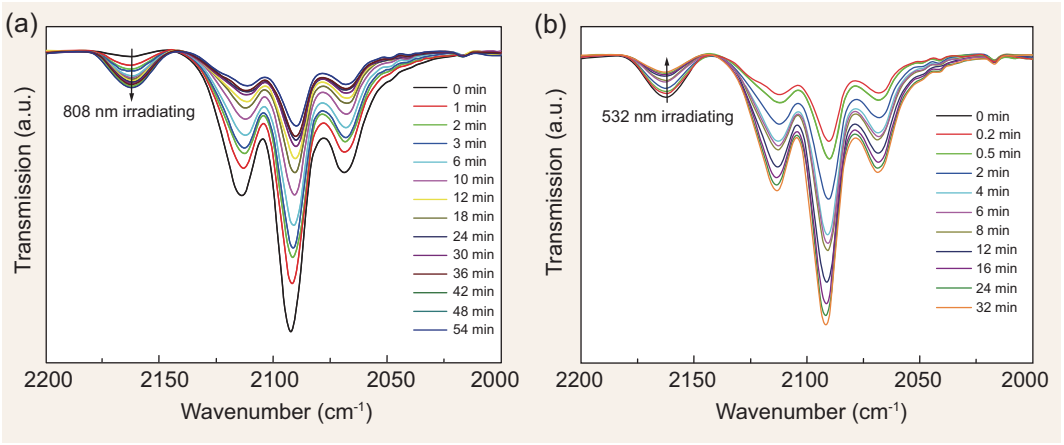

Figure 6. Photo-induced IR spectra for **1a**. Irradiation-time dependence of the IR spectra for **1a** irradiated at 808 nm (a) and the photoreversibility upon irradiation at 532 nm (b) at 20 K.

have a significant effect on redox potential and may have a significant effect on the intermetallic electron-transfer behavior. Hydrogen bonding as an electron-withdrawing effect can result in the positive shifting of Fe^{II} redox potential [31,33]. Fe^{II} ions are more stable in this situation. Thus, **1·2CH$_3$OH·4H$_2$O** exhibits stable $\{Fe^{II}_{LS}(\mu\text{-}CN)Co^{III}_{LS}\}$ linkages in the solvated phase. When **1·2CH$_3$OH·4H$_2$O** loses the solvent molecules and transforms into the desolvated phase **1**, the hydrogen bonding is destroyed, accompanied by a negative shift in the redox potential of Fe^{II}. The $\{Fe^{II}_{LS}(\mu\text{-}CN)Co^{III}_{LS}\}$ linkages become unstable and tend to transform into the $\{Fe^{III}_{LS}(\mu\text{-}CN)Co^{II}_{HS}\}$ linkages. Therefore, the electron transfer from **1·2CH$_3$OH·4H$_2$O** to **1** occurs as a result of thermally induced desolvation.

Second, the average distances of $\pi\cdots\pi$ and C—H$\cdots\pi$ interactions between the adjacent dpq/^{Pz}Tp ligands are 3.753 and 3.148 Å for **1·2CH$_3$OH·4H$_2$O**, 3.665 and 3.102 Å for **1** and 3.457 and 3.002 Å for **1a**, indicating that the interactions gradually become stronger from **1·2CH$_3$OH·4H$_2$O** to **1** and **1a**. The enhancement of intermolecular interactions increases the synergistic effects between molecules and causes an energy decrease to a more stable structure, providing an important driving force for the successive two-step irreversible SCSC transformations. In comparison, only polycrystalline powder **1a** can be obtained directly using solvothermal conditions at 100°C starting from the precursors, as confirmed by powder XRD analyses (see Supplementary Fig. 16). This results show the importance of successive crystalline transformations.

In addition, the coordination spheres of cobalt centers bring out different distortion accompanying the changes in intermolecular interactions (C–H$\cdots\pi$ and $\pi\cdots\pi$) between dpq ligands. This can be observed directly in the deviation of the Co–N≡C bond angles (see Supplementary Table 3). Compared with the bond angles [171.8(5) and 168.6(6)°] in **1·2CH$_3$OH·4H$_2$O**, the difference value (8.9°) of the bond angles [171.1(6) and 162.2(7)°] in **1** is larger, indicating larger deviation from the ideal octahedron for the latter. For **1a**, the bond angles [166.1(3) and 166.7(3)°] are nearly the same, which suggests that the distortion of the CoN_6 octahedron becomes smaller. Continuous shape measurements (CShM) analysis and the parameter Σ (the sum of $|90-\alpha|$ for the 12 *cis*-N–Co–N angles around the Co atoms) were also calculated (see Supplementary Table 2). The CShM of cobalt is 0.178 (**1·2CH$_3$OH·4H$_2$O**), 1.014 (**1**), 0.276 (LT phase of **1a**) and 1.216 (HT phase of **1a**), respectively. A smaller value is generally associated with a stronger ligand field, leading to an LS state of the metal ion, whereas the larger value corresponds to a weaker ligand field and support an HS state. From **1·2CH$_3$OH·4H$_2$O** to **1** and **1a**, the values first increase and then decrease, which suggests that the strength of the ligand field changes from strong to weak and back to strong. Thus, the Co ion exhibits HS state in **1** and the LS state in **1·2CH$_3$OH·4H$_2$O** and **1a**. This unusual behavior serves to illustrate how subtle change in C–H$\cdots\pi$ and $\pi\cdots\pi$ interactions can actually have a profound effect on SCSC transformations and electron-transfer properties.

CONCLUSION

The enhancement of intermolecular $\pi\cdots\pi$ interactions drives successive single-crystalline transformations and achieves three crystalline

phases with different electron-transfer behaviors. Especially, this is the first time that the crystalline transformation between two polymorphs in intermetallic electron-transfer-related compounds has been observed, providing an ideal platform to study the effect of intermolecular $\pi\cdots\pi$ interactions on crystalline-transformation-induced change in electron-transfer behaviors. The introduction of $\pi\cdots\pi$ interactions not only provides a strategy to manipulate the crystalline phases, but also offers access to construct switchable multifunctional materials displaying stimuli-induced dynamic-changes functions in the future.

METHODS

The detailed preparation and characteristic methods of materials are available as Supplementary data at *NSR* online.

SUPPLEMENTARY DATA

Supplementary data are available at *NSR* online.

FUNDING

This work was partly supported by the National Natural Science Foundation of China (91422302, 21421005 and 21322103) and the Fundamental Research Funds for the Central Universities, China.

REFERENCES

1. Salvador JR, Guo F and Hogan T *et al.* Zero thermal expansion in YbGaGe due to an electronic valence transition. *Nature* 2003; **425**: 702–5.
2. Long Y-W, Hayashi N and Saito T *et al.* Temperature-induced A–B intersite charge transfer in an A-site-ordered $LaCu_3Fe_4O_{12}$ perovskite. *Nature* 2009; **458**: 60–3.
3. Akimov AV, Neukirch AJ and Prezhdo OV. Theoretical insights into photoinduced charge transfer and catalysis at oxide interfaces. *Chem Rev* 2013; **113**: 4496–565.
4. Bernardo B, Cheyns D and Verreet B *et al.* Delocalization and dielectric screening of charge transfer states in organic photovoltaic cells. *Nat Commun* 2014; **5**: 3245.
5. Horiuchi S, Okimoto Y and Kumai R *et al.* Quantum phase transition in organic charge-transfer complexes. *Science* 2003; **299**: 229–32.
6. Alves H, Molinari AS and Xie H-X *et al.* Metallic conduction at organic charge-transfer interfaces. *Nat Mater* 2008; **7**: 574–80.
7. Huang Z-X, Auckett JE and Blanchard PER *et al.* Pressure-induced intersite Bi–M (M = Ru, Ir) valence transitions in hexagonal perovskites. *Angew Chem Int Ed* 2014; **53**: 3414–7.
8. Sato O, Tao J and Zhang Y-Z. Control of magnetic properties through external stimuli. *Angew Chem Int Ed* 2007; **46**: 2152–87.
9. Sato O. Dynamic molecular crystals with switchable physical properties. *Nat Chem* 2016; **8**: 644–56.
10. Jeen H, Choi WS and Biegalski MD *et al.* Reversible redox reactions in an epitaxially stabilized $SrCoO_x$ oxygen sponge. *Nat Mater* 2013; **12**: 1057–63.
11. Aguilà D, Prado Y and Koumousi ES *et al.* Switchable Fe/Co prussian blue networks and molecular analogues. *Chem Soc Rev* 2016; **45**: 203–24.
12. Hoshino N, Iijima F and Newton GN *et al.* Three-way switching in a cyanide-bridged [CoFe] chain. *Nat Chem* 2012; **4**: 921–6.
13. Sato O, Iyoda T and Fujishima A *et al.* Photoinduced magnetization of a cobalt-iron cyanide. *Science* 1996; **272**: 704–5.
14. Berlinguette CP, Dragulescu-Andrasi A and Sieber A *et al.* A charge-transfer-induced spin transition in the discrete cyanide-bridged complex $\{[Co(tmphen)_2]_3[Fe(CN)_6]_2\}$. *J Am Chem Soc* 2004; **126**: 6222–3.
15. Li D-F, Clérac R and Roubeau O *et al.* Magnetic and optical bistability driven by thermally and photoinduced intramolecular electron transfer in a molecular cobalt-iron prussian blue analogue. *J Am Chem Soc* 2008; **130**: 252–8.
16. Zhang Y-Z, Li D-F and Clérac R *et al.* Reversible thermally and photoinduced electron transfer in a cyano-bridged $\{Fe_2Co_2\}$ square complex. *Angew Chem Int Ed* 2010; **49**: 3752–6.
17. Nihei M, Sekine Y and Suganami N *et al.* Controlled intramolecular electron transfers in cyanide-bridged molecular squares by chemical modifications and external stimuli. *J Am Chem Soc* 2011; **133**: 3592–600.
18. Mondal A, Li Y-L and Seuleiman M *et al.* On/off photoswitching in a cyanide-bridged $\{Fe_2Co_2\}$ magnetic molecular square. *J Am Chem Soc* 2013; **135**: 1653–6.
19. Koumousi ES, Jeon IR and Gao Q *et al.* Metal-to-metal electron transfer in Co/Fe prussian blue molecular analogues: the ultimate miniaturization. *J Am Chem Soc* 2014; **136**: 15461–4.
20. Zhang Y-Z, Ferko P and Siretanu D *et al.* Thermochromic and photoresponsive cyanometalate Fe/Co squares: toward control of the electron transfer temperature. *J Am Chem Soc* 2014; **136**: 16854–64.
21. Nihei M, Yanai Y and Hsu IJ *et al.* A hydrogen-bonded cyanide-bridged $[Co_2Fe_2]$ square complex exhibiting a three-step spin transition. *Angew Chem Int Ed* 2017; **56**: 591–4.
22. Nihei M, Okamoto Y and Sekine Y *et al.* A light-induced phase exhibiting slow magnetic relaxation in a cyanide-bridged $[Fe_4Co_2]$ complex. *Angew Chem Int Ed* 2012; **51**: 6361–4.
23. Ohkoshi SI, Tokoro H and Matsuda T *et al.* Coexistence of ferroelectricity and ferromagnetism in a rubidium manganese hexacyanoferrate. *Angew Chem Int Ed* 2007; **46**: 3238–41.
24. Hu J-X, Luo L and Lv X-J *et al.* Light-induced bidirectional metal-to-metal charge transfer in a linear Fe_2Co complex. *Angew Chem Int Ed* 2017; **56**: 7663–8.
25. Zhang J-P, Liao P-Q and Zhou H-L *et al.* Single-crystal X-ray diffraction studies on structural transformations of porous coordination polymers. *Chem Soc Rev* 2014; **43**: 5789–814.

26. Kole GK and Vittal JJ. Solid-state reactivity and structural transformations involving coordination polymers. *Chem Soc Rev* 2013; **42**: 1755–75.
27. Schneemann A, Bon V and Schwedler I *et al.* Flexible metal–organic frameworks. *Chem Soc Rev* 2014; **43**: 6062–96.
28. Li C-P, Chen J and Liu C-S *et al.* Dynamic structural transformations of coordination supramolecular systems upon exogenous stimulation. *Chem Commun* 2015; **51**: 2768–81.
29. Ito H, Muromoto M and Kurenuma S *et al.* Mechanical stimulation and solid seeding trigger single-crystal-to-single-crystal molecular domino transformations. *Nat Commun* 2013; **4**: 2009.
30. Liu D-H, Liu T-F and Chen Y-P *et al.* A reversible crystallinity-preserving phase transition in metal–organic frameworks: discovery, mechanistic studies, and potential applications. *J Am Chem Soc* 2015; **137**: 7740–6.
31. Berlinguette CP, Dragulescu-Andrasi A and Sieber A *et al.* A charge-transfer-induced spin transition in a discrete complex: the role of extrinsic factors in stabilizing three electronic isomeric forms of a cyanide-bridged Co/Fe cluster. *J Am Chem Soc* 2005; **127**: 6766–79.
32. Liu T, Zhang Y-J and Kanegawa S *et al.* Water-switching of spin transitions induced by metal-to-metal charge transfer in a microporous framework. *Angew Chem Int Ed* 2010; **49**: 8645–8.
33. Cao L, Tao J and Gao Q *et al.* Selective on/off switching at room temperature of a magnetic bistable $\{Fe_2Co_2\}$ complex with single crystal-to-single crystal transformation via intramolecular electron transfer. *Chem Commun* 2014; **50**: 1665–7.
34. Wei R-J, Nakahara R and Cameron JM *et al.* Solvent-induced on/off switching of intramolecular electron transfer in a cyanide-bridged trigonal bipyramidal complex. *Dalton Trans* 2016; **45**: 17104–7.
35. De S, Jiménez JR and Li YL *et al.* One synthesis: two redox states. Temperature-oriented crystallization of a charge transfer $\{Fe_2Co_2\}$ square complex in a $\{Fe^{II}LSCo^{III}LS\}_2$ diamagnetic or $\{Fe^{III}LSCo^{II}HS\}_2$ paramagnetic state. *RSC Adv* 2016; **6**: 17456–9.
36. Zheng C-Y, Xu J-P and Yang Z-X *et al.* Factors impacting electron transfer in cyano-bridged $\{Fe_2Co_2\}$ clusters. *Inorg Chem* 2015; **54**: 9687–9.
37. Sagara Y, Yamane S and Mitani M *et al.* Mechanoresponsive luminescent molecular assemblies: an emerging class of materials. *Adv Mater* 2016; **28**: 1073–95.
38. Janiak C. A critical account on π–π stacking in metal complexes with aromatic nitrogen-containing ligands. *J Chem Soc, Dalton Trans* 2000; 3885–96.
39. Siretanu D, Li D-F and Buisson L *et al.* Controlling thermally induced electron transfer in cyano-bridged molecular squares: from solid state to solution. *Chem Eur J* 2011; **17**: 11704–8.